Evaluation of the Interface of Green Bilayer Powder Compact (BPC) of Iron (Fe) Under Different Die Wall Conditions

Syamimi Mohd Yusoff[1]*, Suraya Mohd Tahir[1], Azmah Hanim Mohamed Ariff[1], Eris Elliandy Supeni[1] and Mohd Shamsul Anuar[2]

[1]*Department of Mechanical and Manufacturing Engineering, Universiti Putra Malaysia, 43400 UPM, Serdang, Selangor, Malaysia*
[2]*Department of Process and Food Engineering, Universiti Putra Malaysia, 43400 UPM, Serdang, Selangor, Malaysia*

ABSTRACT

The current work evaluates cross-sectioned green bilayer powder compact (green BPC) of iron (Fe) under different die conditions. At first, finite element-based (FE) simultaneous compaction modelling is used to model the uniaxial, one-sided compaction of the green BPC of Fe and its interface. A Tri-mesh of 0.03 mm and mesh refinement along the interfacial boundary is set up with the condition of each node from both sides of layers (namely lower layer, L and upper layer, U) is mapped precisely to ensure its mutual interconnection along the horizontal edges of interface. Additionally, the modelling part utilised and validated our recently proposed image analysis under the metallographic technique's standard framework. Our approach to model the interface to gain the same effect as from the experimental result of green BPC of Fe is in good agreement. It is significantly found that the use of the lubricated die condition contributed to increasing the local RD distribution along the interface of the green BPC of Fe. In contrast, the distribution is gradually dissuaded from the interface for the unlubricated die condition as the applied height: diameter (H:D) ratio increases.

Keywords: Fe, Finite element, green BPC, H:D ratio, interface, local RD

INTRODUCTION

Powder Metallurgy (PM) compaction is a metal-forming technique to fabricate a metal-based powder compact from loose powder. This PM workpiece is frequently produced at once with one layer and is simply known as a green single powder

compact (or green SPC). PM compaction is well-known for its effectiveness in delivering the near-net shape of green SPC. Thus, any additional machining works are not necessary. Enhancement of the strength of green SPC was proposed by notable investigations and practically implemented by industries such as green machining technique (Kulkarni & Dabhade, 2019) and high-velocity compaction (HVC) (Yuan et al., 2021). Instantly, the use of the PM compaction route is widely contributing to various circles of industries, for instance, automobile (Masooth et al., 2022), composites (Arifin et al., 2022), military products (Santos et al., 2018) and healthcare (Elsayed et al., 2022) industries.

Nevertheless, the friction condition of a die wall is a major cause that deteriorates the homogeneity of produced green SPC under PM compaction, as overviewed by Edosa et al. (2022). Past discoveries on techniques in minimising the effect of friction were elaborated that included the designed compaction technique (Canta & Frunza, 2003; Grigoriev et al., 2019; Wang et al., 2009), the initial determination of powder relative bulk density (RBD) (Radchenko, 2004), critical consideration of determined H:D ratio and geometrical powder compact shape (Cristofolini et al., 2018), the mixing method (Chen et al., 2020) and the layering strategy of green SPC to form green BPC in which pioneered by Sopchak and Misiolek (2000). This layering foundation had launched for up-to-date manufacturing of green BPCs that have been thoroughly designed across different fields specifically to formulate drugs (Bellini et al., 2019), Ti6Al4V/20CoCrMo-highly porous Ti6Al4V biomedical bilayer (Mihalcea et al., 2021), Ti6al4V-Ti6Al4V/30Ta bilayer for orthopaedic application (Chávez et al., 2020), ceramics (Hasan et al., 2019), composites (Wang et al., 2019), machining, cutting and drilling tools (Ojo-kupoluyi et al., 2019). It is also a valuable pattern for generating functionally graded materials (FGMs) (Masooth et al., 2022).

Compared to growing numbers of modelling for other techniques to further predict the density quality of green SPC, progression in green BPC has surprisingly outnumbered since then, in particular, for metals (Rowe & Nikfar, 2017). It is due to difficulty in classical assessment on the percentage of internal porosities that limit the basis in bilayer formulation as a modelling start-up wherever concerning its interface. Therefore, each researcher had to create a physical test on BPCs to truly assess the structural type of interface and its mechanism framework along with doubled compaction steps. They made attempts to discover the calibration of BPC parameters through compaction forces (Abebe et al.,2014), three-point bending (Favrot et al., 1999), four-point bending (Boonyongmaneerat & Schuh, 2006) and flexure (Castrati et al., 2016) experiments are commonly utilised, and certain possible datasets had been presented for each test. Henceforth, the identified type of interfacial structures was released, such as interlocking (or dry binding) for green BPC of Fe (Abebe et al.,2014; Sopchak & Misiolek, 2000), cohesive for pharmaceutical BPC of Microcrystalline Cellulose (MCC) and Sodium Dilactose (SDLac) (Castrati et al., 2016) as well as pharmaceutical BPC of MCC and lactose anhydrate (Chang & Sun, 2019) and adhesive for bilayers of Aluminum Oxide (Al_2O_3) and Tungsten (W) powder compact

(Boonyongmaneerat & Schuh, 2006). Recently, El-Nasr and his team have inspired the design of an imaging technique known as a Computer Vision System (CVS) to easy-in-access the computation of internal porosities of BPC of Fe without being in contact with the powder surface (El-Nasr et al., 2020).

Sinka (2007) modelled the interfacial BPC of MCC layers under a tangential surface model for modelling. Accordingly, an assumption of a friction coefficient of 0.5 between the layers was stated without experimental validation (Sinka, 2007). Meanwhile, Castrati et al. (2016) modelled the diametrical breaking test with the tested interfacial BPC of MCC and SDLac assigned as the cohesive model. On the other hand, Yohannes et al. (2017) suggested discretising the contact model between individual particles on both sides of layers, whereby the contact force model was integrated as elastic and plastic deformation-dependent of deformed particles. Apart from their experiment, Boonyongmaneerat and Schuh (2006) introduced the use of FE-based modelling to handle the discretisation of fractural constitutive equations under the fracture mechanism between composite BPC of Al_2O_3 and W. Since the formed interface between the layers is utilised from different materials and had undergone the sintered process via firing cycles; therefore, the type of interaction is regarded as an adhesive (Boonyongmaneerat & Schuh, 2006). Concerned about the development behaviour of BPC of Tungsten Carbide–Cobalt (WC-Co) -based cermets under high temperatures, Favrot et al. (1999) included an assessment of the interfacial response by implementing factors such as different sizes and percentages of WC and Co, respectively on each layer using FE-based modelling. According to them, the curvature of the mesh rightfully indicated the interface condition of the compressed bilayer. Thus, no assigned model had been addressed for their findings. It was proven through a sectioned image from their conducted experiment through cold compaction. In addition, as mentioned in a previous report by Thomazic and his team, the assigned two layers of WC and Fe were arranged under an axial column shape to each other. Finally, they obtained a homogeneous BPC structure whenever Fe is located as a lower (*L*) layer. The effect of the interface is not significant in their cases, but the density gradient was successfully reduced (Thomazic et al.,2010). Above all, for all types of bilayer powder investigations and evaluation on different mechanical effects, in particular, friction coefficient and other interactions between particles that exist along the horizontal layers of BPC are simply precluded as caused by the ongoing development of advanced characterisation to gain rightful datasets of adhesive-cohesive inter-relation and invalidate the assumption of interfacial friction coefficient. Therefore, the constitutive model and its calibrations become a hotspot for incoming investigations. This situation rather prolonged the progressive modelling of the interface of BPC.

The present research work presents the formation of green BPC of ASC 100.29 Fe powder to visualise the evolution of local RD gradient that focuses on the interface to strengthen the Fe- based workpieces in metal forming industries. It became the metal of

choice, did not require alloying to be useful, and was used to manufacture nails, tools, utensils, agricultural equipment, and weapons. Experimentally, adding a layer of green SPC to make green BPC of Fe is well known to reduce the local RD gradient. However, quantitative-based assessment for local RD distribution and modelling evaluations on the interface of green BPC of Fe is not considered for documentation. Plus, a comparative study on changes under different die wall conditions and height-to-diameter (H:D) ratio of green BPC with constantly applied load compaction of 30 kN and 95 kN for lower, L and upper U layers, respectively, were important to be a highlight, therefore, resulted from variation in local RD distribution can be analysed. As an output, a significant way to strengthen the interface to deliver a robust green BPC of Fe can be emphasised. It can potentially contribute to producing defect-free green BPC of Fe.

MATERIAL AND METHODS

Experimental Methods for Validation

Double Steps of Uniaxial One-Sided Compaction. PM compaction was conducted using a universal testing machine (model 3382, Instron, UK) with a load cell with a 100 kN maximum capacity, as depicted in Figure 1. A lower speed of 2 mm min-1 crosshead was used in this work. To produce the green BPC under lubricated die condition (labelled as sample B), magnesium stearate, MgSn, was used to lubricate the die cavity before starting the compaction test. Otherwise, the green BPC without lubricated die condition will be released (labelled as sample A). Next, 11 g of loose Fe powder for the first layer was prepared and manually filled into the rigid die cavity of 20 mm diameter, D, as seen in Figure 1(a). The initial height of the lower layer, HL, was approximately 10 mm. Consequently, as depicted in Figure 1(b), the minimum load compaction, Fu of 30 kN, was then applied via an upper punch to compact the lower L layer of Fe powder, with the bottom punch in a stationary condition. As a result, the height, HL, is reduced to nearly 5 mm. Prior to the compaction of the upper U layer, as seen in Figure 1(c), another layer of Fe powder is compacted under the maximum load compaction, Fu of 95 kN. As a result, the upper layer of Fe powder will have the same final height, HU of 5 mm, as shown in Figure 1(d). Before the ejection process, the base of the die set tool had been replaced by the ejection container, as seen in Figure 1(e), to extrude the green BPC from the die cavity. Another sample is repeated using the same procedures. Table 1 lists the two types of green BPC produced using the steps of PM compaction.

The Use of Low Speed on Compaction and Ejection Force in the Downward Direction. Since a very small mass of loose Fe powder of 11 g is used, a crosshead speed of 2 mm min⁻1 is then employed on each green BPC to reduce the possibility of capping at the bottom of the green BPC and ensure the bonding of the compressed upper, U layer of Fe powder

Table 1

Samples produced under PM compaction on lower, L and upper U layers of the green BPCs of Fe

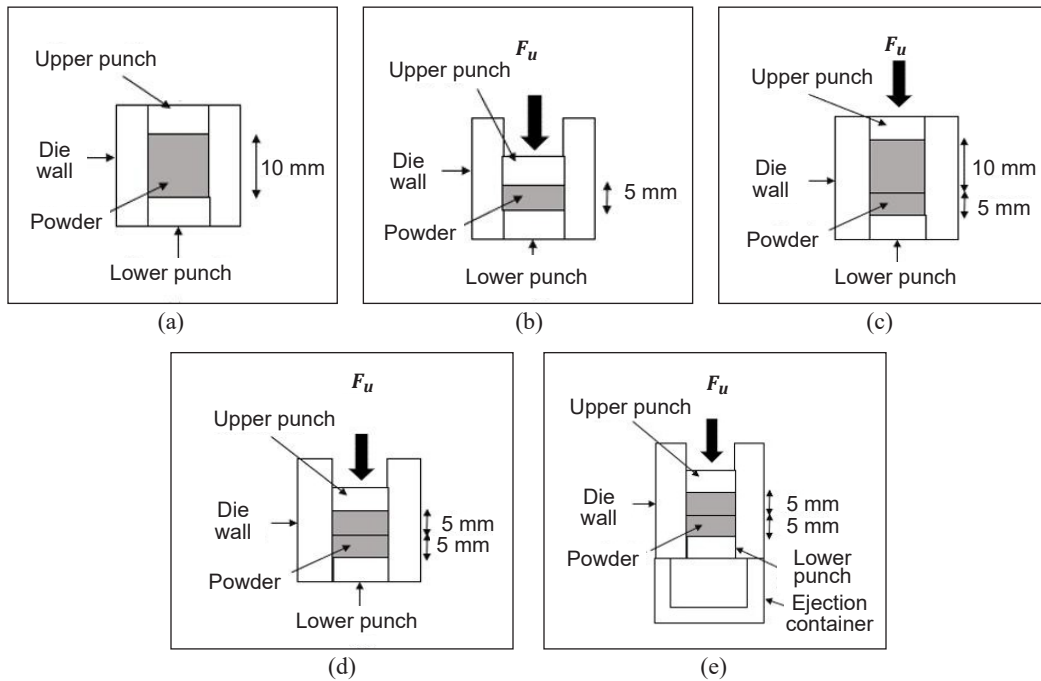| Samples	H:D ratio	MgSn lubricant applied	F_u on L (kN)	F_u on U (kN)
A	1.0	No	30	95
B	1.0	Yes	30	95

Figure 1. PM compaction steps for producing the green BPC of Fe

to the lower, *L* one. Delamination issues can be avoided with the same speed applied for ejection force, thus reducing the impact from the container on its bottom part, as shown in Figure 1(e). Theoretically, the low speed of both compaction and ejection forces hinders the rise of the springback phenomenon. Then, the obtained cylindrical-shaped green BPC with a thickness of 10 mm for sample A and 10 mm for sample B were cross-sectioned following the arranged procedures under a metallographic technique as the authors did (Yusoff et al., 2021). The cross-sectioned were conveniently displayed in Figures 8(a) and 8(b).

Image Analysis Procedures for the Green BPCs. A systematic preparation according to the sequence steps of image analysis procedures from phase to phase 4 in Table 2 was used for validation with the FE-based model to obtain the final local RD distribution across the section of the green BPCs, as in Figure 5. Phase 1 can be represented as per Figures 1(a), 1(b), 1(c), 1(d), and 1(e). The details of phases (2) and (3) were referred to in the previous work of authors (Syamimi et al., 2021).

Table 2

The workflow process to calculate local RD distribution of the cross-sectioned green BPCs of Fe

Phase	Descriptions
(1)	Uniaxial one-sided compaction
(2)	Metallographic methods, including grinding and polishing
(3)	(a) The cross-section of the green BPC with a final thickness of 10 mm (5 mm for both upper, *U* and lower, *L* layers) is indicated in Figure 1(e). Next, under a magnification of 100X, a total of 525 TIF-based pictures were snapped by the camera through the Olympus BX51 software.
	(b) TIF-based pictures were converted into binary images separately via MATLAB software, as shown in Figure 2.
	(c) A Fortran code was developed to create a uniform rectangular grid representing a magnification size of 100X. In addition, a centre-point coordinate (marked as a small red dot colour on each centre of the element) was located within the element size of 0.68 mm and 0.40 mm in the x-direction and y-direction, respectively. Tecplot software has been used to visualise the data retrieved from Fortran in the form of.DAT file. The result of visualisation is indicated in Figure 3. The dimensions are given in this rectangular grid's x- and y- directions were based on the final thickness of the compressed green BPC of sample B in millimetres (mm).
(4)	Under this phase, a one-to-one mapping procedure was performed whereby a binary image of sample B was located backwards of the transparent visualised grid, as displayed in Figure 4.
	The Origin Lab software was employed to map the part from a result of RD calculation obtained in the previous phase into the specified colourised contour. Specific areas with labelled RD distribution are shown in Figure 5 to indicate the selected areas as major distribution levels.

Figure 2. A resulting binary image from TIF-based pictures after conversion with MATLAB software
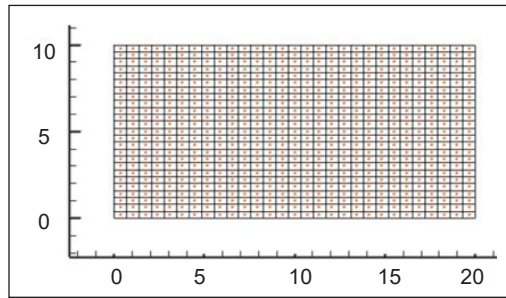

Figure 3. The visualisation of the regular grid arrangement in Tecplot as a result of the performed algorithm in Fortran software
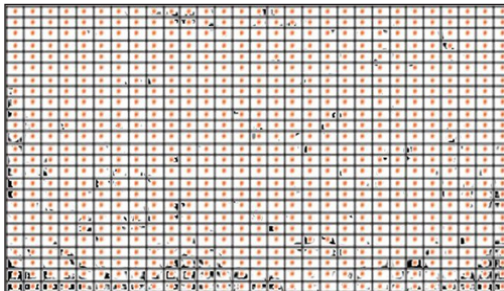

Figure 4. A one-to-one mapping procedure was performed manually in each region of elements that covered the bilayer sample
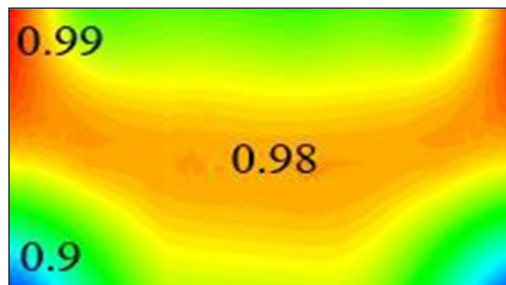

Figure 5. The Origin Lab displayed the resulting contour of RD values

Development of Simultaneous Compaction Model Using FE-Based Modelling

Geometrical Model for Green BPC Compaction. An axisymmetric geometrical model was set up similarly in the experiment to compact the loose Fe powder of ASC 100.29 simultaneously in Abaqus 6.20. Initially, the height H of undeformed Fe powder is 10 mm. In addition, the pair of punches is always set as same as the die mould's radius of 10 mm. Therefore, the length, $l,$ for each punch's length is 10 mm. Finally, the height, $H_d,$ of the die wall is set to follow the height, $H,$ of undeformed Fe powder

FE Parameters for Variation in H:D Ratios. To further analyse the changes in interfacial local RD distribution concerning the changes in height, H (mm) of the powder layer, an implementation of measurement through the H:D ratio is conducted. As indicated in Table 3, H:D ratios of 1.0, 1.3, and 1.6 are selected, whereby each height of lower, H_L and upper H_U layers of green BPC are set. A load of compaction, F_u (kN) applied is 30 kN for the lower layer, L and 95 kN upper layer, U. For all H:D ratios, modelling procedures are applied in each module starting from part and assembly, followed by the property, mesh, step module and finally the job modules in Abaqus 6.20. All the modules were done in similar ways with the same data. An exception had been granted only for the changes in heights of lower, H_L and upper H_U layers of Fe powder parts.

Table 3
List of H:D ratios under a load of compaction, F_u for green BPCs of Fe of samples A, B, C and D

Samples of green BPC	H:D ratio	H_L (mm)	H_U (mm)	F_u on L (kN)	F_u on U (kN)
A	1.0	10	10	30	95
B	1.0	10	10	30	95
C	1.3	13	13	30	95
D	1.6	16	16	30	95

Mesh. Despite using Quad dominated-based mesh on the Fe powder layer, a Tri-based mesh is important to utilise both layers of the modelled green BPC with the main element under the size of 0.03 mm. With a correct mapping towards the boundary interface, approximately 100 seedings were used to refine the Tri-based mesh from both sides of the layer. This description can be visualised in Figure 6.

The Properties of Green BPCs of Fe. Ranging from Modulus, E to Yield Stress, p_s, the properties of ASC 100.29 Fe powder as the material of formed green BPC serve as input parameters of built-in Drucker-Prager Cap (DPC) model with an initial local RD of 35 gmm^{-3} or 0.5 and final local RD of 70 gmm^{-3} or 1.0. Table 4 contained the properties in which processing under the property module in Abaqus 6.20 for PM compaction. The Brewin equations calculate the data (Brewin et al., 2007).
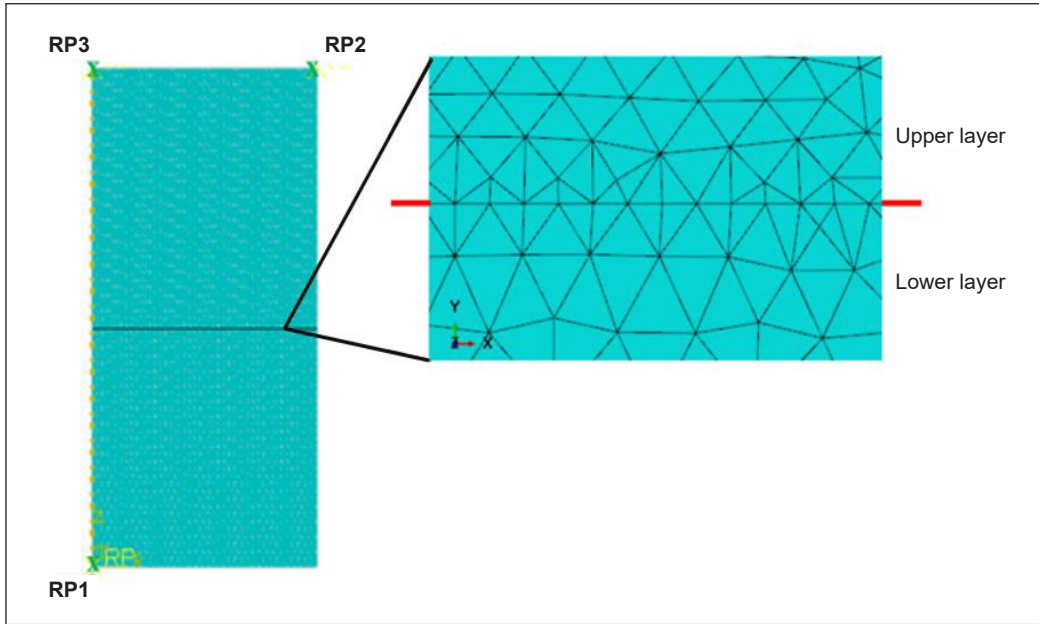
Figure 6. An arrangement of an FE-based model for undeformed green BPC modelling with a close-up of precisely connected nodes between both sides of layers. The red side lines indicate an actual boundary of an interface between two compressed layers of Fe

Table 4
List of input parameters for modelled green BPCs of Fe using the built-in Drucker-Prager Cap (DPC) model

Local RD	Modulus E (MPa)	Poisson Ratio v	Cohesiveness c (MPa)	Angle of Repose tan f	Cap eccentricity C	Yield stress ps (MPa)	Plastic Strain εpl
0.5	5644.12	0.0556	0.001	72.48784	0.56465685	12.89	0
0.55	7752.25	0.0607	0.2485472	72.05262	0.57774487	24.78	0.3738570
0.7	16317.06	0.0909	3.0391120	70.85212	0.66822970	110.1	0.6150191
0.75	21301.68	0.1059	6.1909922	70.47973	0.72582784	165.8	0.6840119
0.8	29109.18	0.1234	12.040375	70.11856	0.80407416	242.6	0.7485505
0.85	42633.40	0.1433	22.486328	69.76742	0.90835824	346.2	0.8091751
0.9	68727.35	0.1658	40.517986	69.42531	1.04501934	483.6	0.8663335
0.95	125703.4	0.1907	70.717656	69.09136	1.22144311	662.9	0.9204007
1.0	270046.3	0.2182	119.94670	68.76484	1.44616171	893.7	0.9716940
0.7	16317.06	0.0909	3.0391120	70.85212	0.66822970	110.1	0.6150191
0.75	21301.68	0.1059	6.1909922	70.47973	0.72582784	165.8	0.6840119
0.8	29109.18	0.1234	12.040375	70.11856	0.80407416	242.6	0.7485505
0.85	42633.40	0.1433	22.486328	69.76742	0.90835824	346.2	0.8091751
0.9	68727.35	0.1658	40.517986	69.42531	1.04501934	483.6	0.8663335
0.95	125703.4	0.1907	70.717656	69.09136	1.22144311	662.9	0.9204007
1.0	270046.3	0.2182	119.94670	68.76484	1.44616171	893.7	0.9716940

FEM Parameters for Variation in Die Wall Condition in Terms of Friction Coefficient, μ. In Abaqus 6.20, the selected interactions are manually done under the interaction module. It includes the first interaction, assigned between the lower punch and the bottom side of the Fe powder lower layer. It is followed by the second interaction, which consists of the die surface and the side of the Fe powder lower layer and the third interaction, between the die surface and the side of the Fe powder upper layer. In addition, the fourth interaction consists of the upper side of the Fe powder upper layer and the lower side of the upper punch. Lastly, the fifth interaction is between the upper side and the lower side of the lower and upper layers of Fe powder, respectively. The location of each interaction is seen in Figure 7.

Consequently, in Tables 5 and 6, each interaction was assigned with friction coefficient values, μ, by applying one of the available mechanical constraint formulations in Abaqus 6.20, namely the penalty contact method. The penalty contact method is a type of contact property that falls under tangential contact surfaces. To model the interface of

Figure 7. Each side is numbered to indicate the area used to define the interactions involved in the modelling of the green BPCs of Fe

undeformed green BPC under the lubricated die condition, a value of friction coefficient, μ of 0.08, is used. Whereas for the modelling under the unlubricated die condition, a value of friction coefficient, μ of 0.18, is used. For unlubricated surfaces, such as indicated under interactions of 1 and 4 for the green BPC of the Fe model, a selected value of friction coefficient, μ of 0.5, is used.
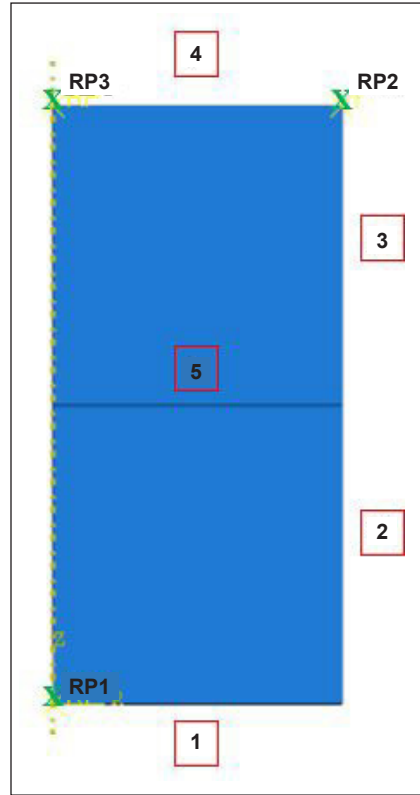
Table 5
List of employed values for friction coefficient, μ for the green BPC of Fe (sample A) under unlubricated die condition

Number of interactions	μ
1	0.5
2	0.18
3	0.18
4	0.5
5	0.08

Table 6
List of employed values for friction coefficient, μ for the green BPC of Fe (sample B) under lubricated die condition

Number of interactions	μ
1	0.5
2	0.08
3	0.08
4	0.5
5	0.08

RESULTS AND DISCUSSION

Few dissimilarities of local RD distribution are found between the sectioned of the green BPCs of sample A (unlubricated) and B (lubricated with MgSn). As referred to the left of Figures 8(a) and 8(b), both samples mutually appeared smooth around their mid-region and the uppermost corner of green BPCs of Fe regions. In contrast, the lowermost corner regions were visibly gloomy in colour. These results are fundamentally consistent with the works of Rajab and Coleman (1985), Sopchak and Misiolek (2000) and Zadeh (2010) for ASC 100.29 Fe powder. Theoretically, the Fe powder particles positioned nearer to the die wall and upper punch tend to densify and re-arrange as the compaction force is further applied in the gravitational direction. Meanwhile, the darkening regions were deteriorated by randomly distributed porosities and less received the effect of densification from the upper punch.

However, sample A's mid-region is devoted to having few scattered porosities. At the same time, sample B's mid-region is almost impossible to have any physically observed porosities. Therefore, it is essential to use a high magnification of 100X under the optical microscope to gain details measurements regarding local RD distribution across the section of green BPCs. As an outcome, the experimental contour for local RD distribution is displayed on the right of Figures 8(a) and 8(b). A large range between 0.82 and 0.99 is displayed by sample A under unlubricated die condition, whereas a short range between 0.9 and 0.99 is displayed by sample B.
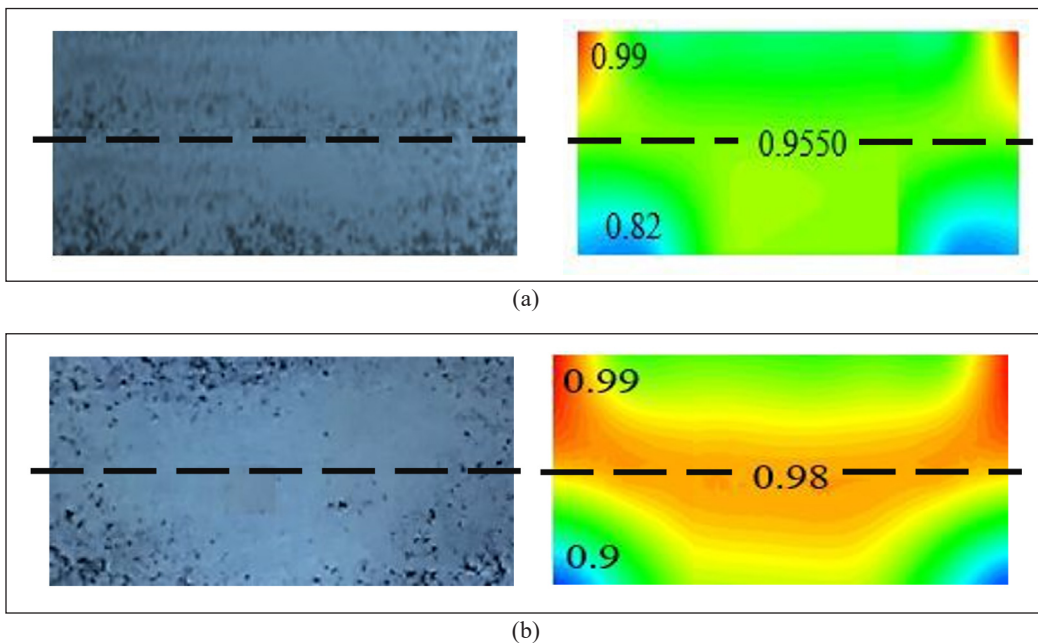

(a)

(b)

Figure 8. Experimental local RD distributions obtained for a whole geometrical shape of green BPCs of Fe: (a) Sample A; and (b) Sample B

Validation of the Axisymmetric FE-Based Modelling

The modelling of PM compaction for green BPC of samples A and B is validated with the experimental results (Figure 9). It is found that, under the modelling part, the unlubricated die condition delivered a large gradient of local RD distribution within sample A, indicated by the solution-dependent variable (SDV1) contour. Compared to the experimental result, each value under the three main regions of the uppermost and lowermost corners and the mid-region are nearer to the modelling results by only differences of 0.79%, 2.27% and 0.79%, correspondingly. Differing to sample B, a small gradient of local RD distribution is captured under lubricated die condition. Indeed, the only differences between the experiment and modelling were only 0.21%, 1.5% and 0.52% for regions of the uppermost and lowermost corner and mid-region, respectively. The validation is conveniently achieved by satisfying the basic work on evaluation under PM compaction, whereby the difference in percentages with less than 5.0% is allowable (Tweed et al., 2008).
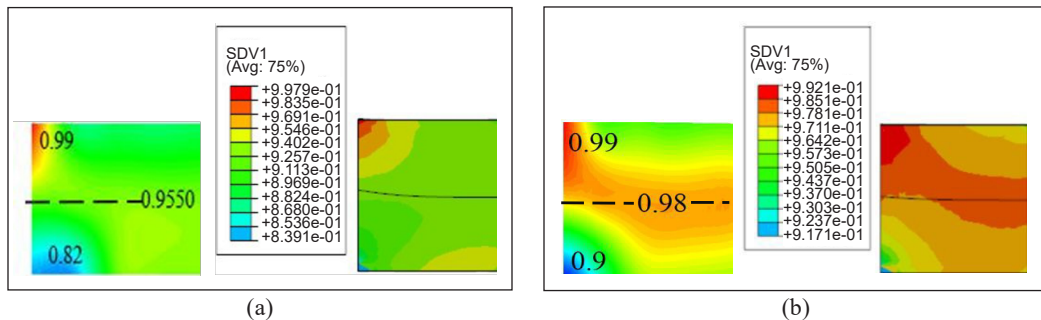

Figure 9. Comparison of RD distributions obtained from experimental work (left) and FE (right) for (a) sample A and (b) sample B of green BPCs of Fe

Mesh Convergence and Sensitivity Analysis

A mesh convergence study was performed to determine the optimal element size. The relative density convergence plot of eight different element sizes is displayed in Figure 10. It was found that an element size of 0.03 mm was able to produce a converged solution within a reasonable period. Previous agreements and their convergence have given confidence in the predictive capabilities of the proposed model (for compaction).

In Equation 1, 0.98 is an obtained value of local RD from the experiment. Using the largest tri-element size of 0.5 mm on the upper and lower layers recorded large errors between FEM and the experimental values with errors of 0.035. Finally, using the smallest size of 0.1 mm with 110 total seedings, a nearer value of interfacial local RD is obtained, as indicated in Figure 11. A good prediction of local RD values in other region parts was also obtained, similar to the good prediction at the interface.

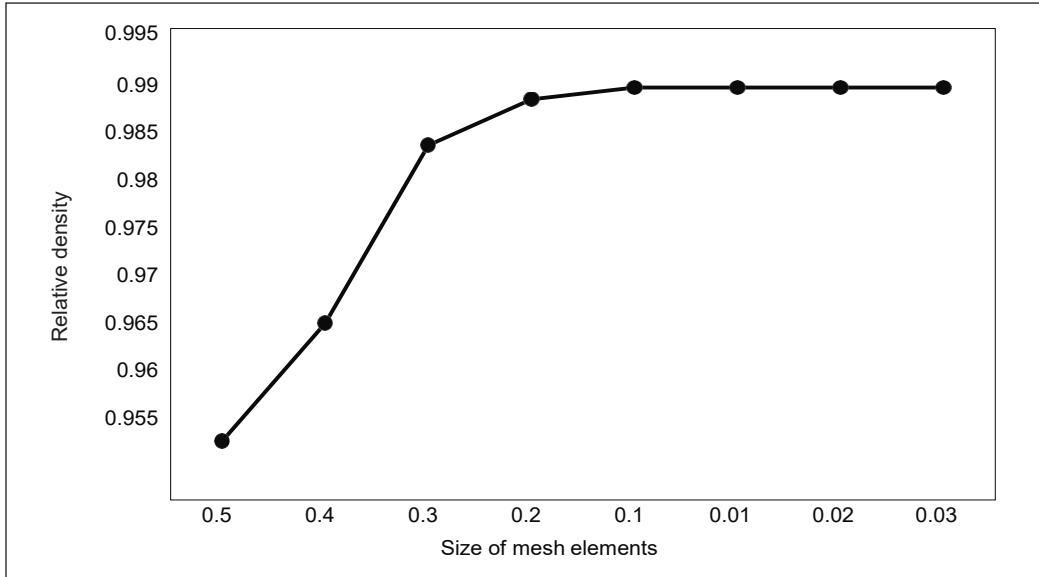$$Error(\Delta) = Value\ of\ local\ RD\ at\ the\ interface\ (FE) - 0.98 \qquad (1)$$
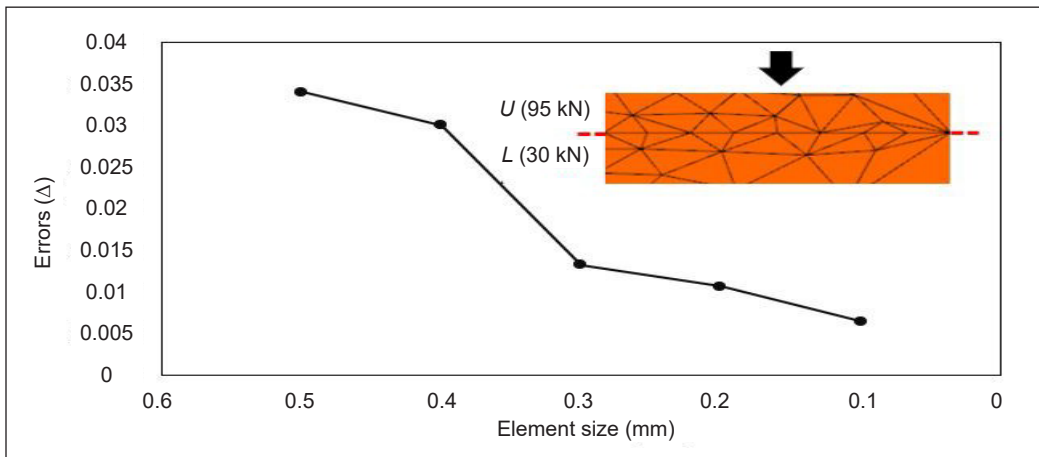
Figure 10. Mesh convergence analysis

Figure 11. A graph of errors against element sizes (in mm). A picture inside indicated a close-up of the interface of the green BPC of Fe at the final compaction stage with a precise connection between its nodes

Local RD Distributions for Variation in H/D Ratios of the Green BPC of Fe Under Different Applied Friction Coefficients

In Figures 12(a), 12(b) and 12(c), two modelled green BPC of Fe with their corresponding H:D ratios of 1.0, 1.3 and 1.6 were compared under different die conditions. The left and right of Figure 12 show the unlubricated and lubricated die results with applied friction coefficient values, μ equal to 0.18 and 0.08, respectively. In Figure 12(a), the green BPC under lubricated die condition had enhanced its local RD distribution within the average of 0.9816 along the interface with the range of local RD distribution between 0.9781 and

0.9851. It is noticed that the interfacial densification within the green BPC that was compressed under the unlubricated die condition had not emerged with a recorded higher range between 0.9402 and 0.9546.

Same in Figure 12(b), the compressed green BPC of Fe with an H:D ratio of 1.3 did not receive the densification support along its interfacial region under the unlubricated die condition with local RD distribution slightly reducing within the range between 0.9323 and 0.9456. Compared to the green BPC of Fe that was compressed under the lubricated die condition, significant horizontal densification is discovered between the two layers within an increased average of 0.98. In addition, it resulted in the local RD distribution within the range between 0.9817 and 0.9882.

As Figure 12(c) observed, the unlubricated die condition had delivered unfamiliar distribution of local RD right below its interface with captured average values of 0.9686. For the green BPC of Fe under the lubricated die condition, an

(a)

(b)

(c)

Figure 12. Contour results of local RD distribution for H:D ratios of (a) 1.0, (b) 1.3, and (c) 1.6

increase of its local RD distribution is seen along its horizontal interface but less covered on its lower layer. With the increase of powder thickness with an H:D ratio of 1.6 under the unlubricated die condition, higher local RD distribution formed along the side of the die wall. Consequently, extended densification of powder particles is seen localised at the middle region of the lower layer and thus creates discontinuity of distributed local RD values between two compressed layers. Current findings are consistent with the results reported by previous literature whereby the mid-region of formed green BPC under unlubricated die condition is lower compared to the regions nearer to the side of the die wall.

CONCLUSION

This evaluation on the interface of green bilayer powder compact (BPC) of iron (Fe) under two different die wall conditions provides both qualitative and quantitative insights
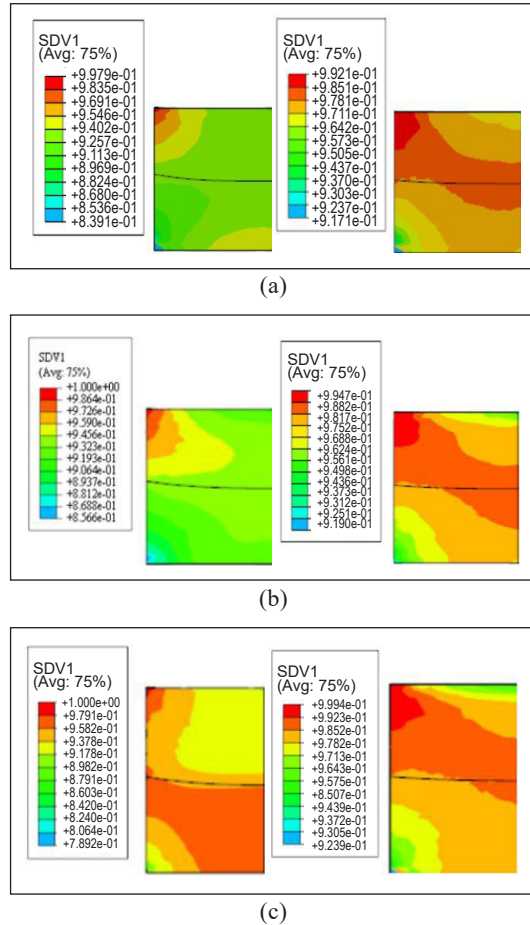
into distributions of the local relative density (or local RD). The study revealed that axial friction from the die wall under unlubricated die conditions had disrupted the flowability of the compressed upper U layer onto the lower L layer of Fe to form an interlocking type of densification. Whereas lubricated die condition supported the interface of BPC whereby less friction from the die wall had allowed for the flowability and promoted an interlocking between compressed upper, U layer onto lower, L layer of Fe during the second time of PM compaction. This condition would strengthen the bilayer system and reduce the local RD gradient across its internal cross-sectioned. The FE-based simultaneous compaction modelling results suggest that the nodes along the interfacial boundary between upper, U- and lower, L- surface layers of BPC of Fe must be in mutual interconnection to gain the interlocking (or dry binding) effect in which similarly obtained in experimental results. Also, the modelling study showed that the increment of height to diameter (H:D) ratio with constantly applied load magnitude had released less interlocking effect from the upper to lower part of the BPC structure. It is estimated that the increase in load magnitude must be done proportionally for both layers, i.e., 60 kN and 190 kN for upper, U- and lower, L- surface layers, respectively, to get the mid-interlocking effect which will help minimise the local gradient as H:D ratio is increased. In addition, it is evidenced that using input parameters from Brewin equations with the medium of built-in DPC in Abaqus 6.20 agrees well with the experimental results of local RD with the condition that the tri-based mesh elements with refinement along the interface must be provided. Also, the selection of friction coefficient, μ of 0.08 and 0.18 to denote the lubricated and unlubricated die wall conditions, respectively, is proved suitable, therefore, benefited the establishment of green BPC of the Fe model. It can potentially contribute to producing defect-free green layered Fe powder compacts.

ACKNOWLEDGEMENT

REFERENCES

Abebe, A., Akseli, I., Sprockel, O., Kottala, N., & Cuitiño, A. M. (2014). Review of bilayer tablet technology. *International Journal of Pharmaceutics*, *461*(1-2), 549-558. https://doi.org/10.1016/j.ijpharm.2013.12.028

Arifin, A., Gunawan, G., & Yani, I. (2022). *Plagiarism and similarity checker of porous titanium alloy/ hydroxyapatite composite using powder compaction route*. Turnitin Universitas Sriwiajaya. https:// repository.unsri.ac.id/66950/

Bellini, M., Walther, M., & Bodmeier, R. (2019). Evaluation of manufacturing process parameters causing multilayer tablets delamination. *International Journal of Pharmaceutics*, *570*, Article 118607. https://doi. org/10.1016/j.ijpharm.2019.118607

Boonyongmaneerat, Y., & Schuh, C. A. (2006). Contributions to the interfacial adhesion in co-sintered bilayers. *Metallurgical and Materials Transactions A*, *37*(5), 1435-1442. https://doi.org/10.1007/s11661-006-0088-9

Brewin, P. R., Coube, O., Doremus, P., & Tweed, J. H. (2008). *Modelling of Powder Die Compaction* (Vol. 329). Springer.

Canta, T., & Frunza, D. (2003). Friction-assisted pressing of PM components. *Journal of Materials Processing Technology*, *143-144*, 645-650. https://doi.org/10.1016/S0924-0136(03)00475-8

Castrati, L., Mazel, V., Busignies, V., Diarra, H., Rossi, A., Colombo, P., & Tchoreloff, P. (2016). Comparison of breaking tests for the characterization of the interfacial strength of bilayer tablets. *International Journal of Pharmaceutics*, *513*(1-2), 709-716. https://doi.org/10.1016/j.ijpharm.2016.10.005

Chang, S. Y., & Sun, C. C. (2019). Effect of particle size on interfacial bonding strength of bilayer tablets. *Powder Technology*, *356*, 97-101. https://doi.org/10.1016/j.powtec.2019.07.100

Chávez, J., Jiménez Alemán, O., Flores Martínez, M., Vergara-Hernández, H. J., Olmos, L., Garnica-González, P., & Bouvard, D. (2020). Characterization of Ti_6Al_4V–$Ti_6Al_4V/30Ta$ bilayer components processed by powder metallurgy for biomedical applications. *Metals and Materials International*, *26*(2), 205-220. https://doi.org/10.1007/s12540-019-00326-y

Chen, W., Wang, J., Wang, S., Chen, P., & Cheng, J. (2020). On the processing properties and friction behaviours during compaction of powder mixtures. *Materials Science and Technology (United Kingdom)*, *36*(10), 1057-1064. https://doi.org/10.1080/02670836.2020.1747779

Cristofolini, I., Molinari, A., Pederzini, G., & Rambelli, A. (2018). From experimental data, the mechanics relationships describing the behaviour of four different low alloyed steel powders during uniaxial cold compaction. *Powder Metallurgy*, *61*(1), 10-20. https://doi.org/10.1080/00325899.2017.1361507

Edosa, O. O., Tekweme, F. K., & Gupta, K. (2022). A review on the influence of process parameters on powder metallurgy parts. *Engineering and Applied Science Research*, *49*(3), 433-443.

El-Nasr, A. A., Saleh, A., & Alshennawy, A. A. (2020). Porosity measurement of iron oxide by using computer vision system. *International Journal of Engineering Research and Technology, 13*(4), 653-659.

Elsayed, M. M., Aboelez, M. O., Mohamed, M. S., Mahmoud, R. A., El-Shenawy, A. A., Mahmoud, E. A., Al-Karmalawy, A. A., Santali, E. Y., Alshehri, S., Elsadek, M. E. M., El Hamd, M. S., & Ramadan, A. E. H. (2022). Tailoring of rosuvastatin calcium and atenolol bilayer tablets for the management of hyperlipidemia associated with hypertension: a preclinical study. *Pharmaceutics*, *14*(8), Article 1629.

Favrot, N., Besson, J., Colin, C., & Delannay, F. (1999). Cold Compaction and Solid-State Sintering of WC-Co-Based Structures: Experiments and Modeling. *Journal of the American Ceramic Society*, *82*(5), 1153-1161. https://doi.org/10.3390/pharmaceutics14081629

Grigoriev, S. N., Dmitriev, A. M., Korobova, N. V., & Fedorov, S. V. (2019). A cold-pressing method combining axial and shear flow of powder compaction to produce high-density iron parts. *Technologies*, *7*(4), 2-17. https://doi.org/10.3390/technologies7040070

Hasan, M., Zhao, J., Huang, Z., Wei, D., & Jiang, Z. (2019). Analysis and characterization of WC-10Co and AISI 4340 steel bimetal composite produced by powder-solid diffusion bonding. *The International Journal of Advanced Manufacturing Technology*, *103*(9), 3247-3263. https://doi.org/10.1007/s00170-019-03709-y

Kulkarni, H., & Dabhade, V. V. (2019). Green machining of powder-metallurgy-steels (PMS): An overview. *Journal of Manufacturing Processes*, *44*, 1-18. https://doi.org/10.1016/j.jmapro.2019.05.009

Masooth, P. H. S., Bharathiraja, G., Jayakumar, V., & Palani, K. (2022). Microstructure and mechanical characterisation of ZrO_2 reinforced Ti_6Al_4V metal matrix composites by powder metallurgy method. *Materials Research Express*, *9*(2), Article 020003. https://doi.org/10.1088/2053-1591/ac5352

Mihalcea, E., Vergara-Hernández, H. J., Jimenez, O., Olmos, L., Chávez, J., & Arteaga, D. (2021). Design and characterization of $Ti_6Al_4V/20CoCrMo−$ highly porous Ti_6Al_4V biomedical bilayer processed by powder metallurgy. *Transactions of Nonferrous Metals Society of China*, *31*(1), 178- 192. https://doi.org/10.1016/S1003-6326(20)65486-3

Ojo-kupoluyi, O. J., Tahir, S. M., Hanim, M. A., Anuar, M. S., & Dele-Afolabi, T. T. (2019). Investigating the effect of sintering temperature on the microstructure and hardness of cemented tungsten carbide/steel bilayer. *IOP Conference Series: Materials Science and Engineering, 469*(1), Article 012020. https://doi.org/10.1088/1757-899X/469/1/012020

Radchenko, A. K. (2004). Mechanical properties of unsintered pressings. I. phenomenological relations for unsintered pressing strength. *Powder Metallurgy and Metal Ceramics, 43*(9), 447-460. https://doi.org/10.1007/s11106-004-0003-0

Rajab, M., & Coleman, D. S. (1985). Density distributions in complex shaped parts made from iron Powders. *Powder Metallurgy, 28*(4), 207-216.

Rowe, J. M., & Nikfar, F. (2017). Modeling approaches to multilayer tableting. In P. Pandey & R. Bharadwaj (Eds.), *Predictive Modeling of Pharmaceutical Unit Operations* (pp. 229-251). Woodhead Publishing. https://doi.org/10.1016/B978-0-08-100154-7.00009-0

Santos, T. D. E. D. S., Regiani, I., Rocha, R. J., & Rocco, J. A. F. F. (2018). Copper/iron brake friction for military aircraft application. *Journal of Aerospace Technology and Management*, *10*, Article e2018. https://doi.org/10.5028/jatm.v10.834

Sinka, C. (2007). Modelling powder compaction. *KONA Powder and Particle Journal*, *25*, 4-22. https://doi.org/10.14356/kona.2007005

Sopchak, N. D., & Misiolek, W. Z. (2000). Density gradients in multilayer compacted iron powder parts. *Materials and Manufacturing Processes*, *15*(1), 65-79. https://doi.org/10.1080/10426910008912973

Thomazic, A., Guennec, Y. L., Kamdem, Y., Pascal, C., Chaix, J. M., Doremus, P., Imbault, D., Bouvard, D., & Doré, F. (2010, October 10-14). *Fabrication of bimaterial components by conventional powder metallurgy*. [Paper presentation]. In Proceedings of the International Powder Metallurgy World Congress & Exhibition, Florence, Italy.

Wang, J. Z., Qu, X. H., Yin, H. Q., Yi, M. J., & Yuan, X. J. (2009). High velocity compaction of ferrous powder. *Powder Technology*, *192*(1), 131-136. https://doi.org/10.1016/j.powtec.2008.12.007

Wang, L., Wang, D., Huang, S., Guo, X., Wan, G., Fan, J., & Chen, Z. (2019). Controllable shape changing and tristability of bilayer composite. *ACS Applied Materials & Interfaces*, *11*(18), 16881-16887. https://doi.org/10.1021/acsami.8b21214

Yohannes, B., Gonzalez, M., Abebe, A., Sprockel, O., Nikfar, F., Kiang, S., & Cuitiño, A. M. (2017). Discrete particle modeling and micromechanical characterization of bilayer tablet compaction. *International Journal of Pharmaceutics*, *529*(1-2), 597-607. https://doi.org/10.1016/j.ijpharm.2017.07.032

Yuan, X., Qu, X., Yin, H., Feng, Z., Tang, M., Yan, Z., & Tan, Z. (2021). Effects of sintering temperature on densification, microstructure and mechanical properties of al-based alloy by high-velocity compaction. *Metals*, *11*(2), Article 218. https://doi.org/10.3390/met11020218

Yusoff, S. M., Tahir, S. M., Hanim, M. A. A., Supeni, E. E., & Anuar, M. S. (2021). Fabrication and evaluation of density distribution in green bilayer iron powder compact. *Materials and Manufacturing Processes*, *36*(6), 660-667. https://doi.org/10.1080/10426914.2020.1854474

Zadeh, H. K. (2010). *Finite Element Analysis and Experimental Study of Metal Powder Compaction*. Queen's University.